scientific reports



OPEN

Biogenic design of silicious architectures on Moso bamboo culm

Makoto Kazama¹, Hiroto Watanabe¹, Chikako Hasekura², Takumi Wakabayashi¹, Takaaki Ishigure¹, Yuya Oaki¹ & Hiroaki Imai¹⊠

Biosilicas that are produced in vascular plants (plant opal), such as Poaceae, have a variety of shapes and functions and are regarded as an excellent model for the architectural design of artificial amorphous materials. In this work, we studied the micro- and nanostructures and mechanical and optical functions of plant opals on the bamboo culm, which is available as an important natural material. The surface of the culm wall is totally covered with silicified epidermal cells containing silica wedges. The biogenic silicious architectures, such as silicified cell walls and wedges, are composed of nanoscale particles ~ 20–80 nm in diameter with cellulose nanofibrils. Silica wedges, which have a relatively low organic content and relatively high hardness and Young's modulus, are initially formed on cellulose nanofibrils in an organic frame as a scaffold within a few weeks after the emergence of a bamboo shoot. Several months after the formation of the wedges, the epidermal cell walls, which protect the culm surface, are lightly silicified with cellulose nanofibrils. According to a numerical simulation, the silica wedges would have an optical function delivering sunlight to chloroplasts located under the epidermal cells.

A variety of inorganic architectures consisting of calcium carbonate, calcium phosphate, and silica, which are called biominerals, are biogenically produced by organisms under environmental conditions. Specific vital functions emerge from the architectonics of biogenic skeletons and shells that have precisely controlled morphologies. Hierarchical architectures of biominerals are composed of nanoscale grains incorporated with organic polymers, regardless of crystalline and non-crystalline states^{1–5}. The essence of biogenic morphological design has been a fascinating scientific interest with regard to understanding biological mineralization and the unique properties of biological materials. In recent years, widespread applications in artificial systems have been inspired by several interesting biogenic structures^{1,2}.

Hydrated amorphous silica (SiO₂•nH₂O) is widely observed in a variety of living organisms, such as diatoms^{3,6-11}, sponges¹²⁻¹⁵, skeletal protists^{16,17}, and some vascular plants¹⁸⁻²¹. The structures, morphogenetic mechanism, and functions have been studied for a wide variety of biosilicas. Frustules, spicules, and hollow skeletons have been found to have adequately designed hierarchical architectures^{6,7,14}. Since particularly shaped amorphous silicas of Poaseae (plant opals) are interesting because of their variety of shapes and microstructures, the biosilicas that provide excellent mechanical, optical, and defensive functions have been characterized in the leaves of rice plants and bamboos^{13,18,21-27}. Plant opals play an important role in the vital activity of plants in the family Poaceae. Recently, cellulose nanofibrils (CNFs) were found to be essential as a scaffold for silica accumulation in rice husks and leaf blades. Prior to silicification, CNFs ~10 nm wide are sparsely stacked in a space between the epidermal cell wall and the cuticle layer. Silica nanoparticles 20–50 nm in diameter are then deposited in the framework of the CNFs as a scaffold¹⁹. Shape-controlled plant opals are formed through the intrafibrillar mineralization of silica nanoparticles on the CNF framework.

The surfaces of bamboo culm walls are known to be covered with silica-rich layers embedding round plates²⁶. However, details of the micro- and nanostructures and the formation process of the surface silicas have not been clarified sufficiently regardless of the abundant availability of bamboo culm walls as a building and craft material. The round silica plates were suggested to increase a critical stress with prevention of crack propagation on the culm surface by a mechanical simulation²⁷. On the other hand, other vital activity function, such as optical properties, were not discussed for bamboo culm walls.

În this work, we chose to focus on moso bamboo (*Phyllostachys edulis* (Carriére) Houz.), which is one of the largest bamboo species in both Japan and China, has the widest range of uses, and produces the largest amount

¹School of Integrated Design Engineering, Keio University, 3-14-1 Hiyoshi, Kohoku-ku, Yokohama 223-8522, Japan. ²Faculty of Agriculture, Tokyo University of Agriculture, Funako, Atsugi 1737, 243-0034, Japan. [⊠]email: hiroaki@applc.keio.ac.jp

of bamboo culms and shoots. Here, the micro- and nanoscale structures of the siliceous architecture of culm walls were studied using various characterization techniques. The microscale morphology of two kinds of plant opals was investigated in the cortex of bamboo culm walls at various growth steps. After several treatments, the micro- and nanoscale structures were characterized by electron micrography, composition analysis, and various spectroscopies. The variation of the mechanical properties was revealed using the nano-indentation technique. Moreover, the optical function of specifically shaped silicas on the epidermal layer was discussed using numerical simulation. Finally, we succeeded in accurately describing the architectonics of biological silicas in bamboo. The biogenic architectures are regarded as an excellent model for the architectural design of artificial amorphous materials that are utilized for various applications.

Results and discussion

Micrometer-scale morphology of two kinds of plant opals

We used culms and shoots of moso bamboo in the current year (Fig. S1 in the Supporting Information (SI)). Figure 1 shows illustrations and optical and scanning electron micrograph (SEM) images of cross sections of the mature culm wall, which has a laminate structure consisting of a cortex, parenchyma with vascular bundles, and a pith ring (Fig. 1a). The cortex is composed of three layers (epidermis, hypodermis, and transitional layers) (Fig. 1b). The elemental mapping for silicon (Si) on an SEM image (Fig. 1e) indicates that the epidermal layer $\sim 15~\mu m$ thick is silicified. The dark green band in the optical micrograph (Fig. 1c, d) shows that chloroplasts are contained in the hypodermis and transitional layers under the silicified cells. In this work, we focused on biosilicas located in the epidermal layer.

Here, we revealed the micrometer-scale morphology of biosilicas in the cortex. Figure 2 shows illustrations and SEM images of the silicified structures in the epidermal layer. The morphology of biosilica in culms of moso bamboo is basically similar to that of *Phyllostachys bambusoids* Siebold et Zucc. reported in the previous study²⁶. The original surface of the epidermal layer is mostly covered with organic matter, such as cuticular wax (Fig. 2a and Fig. S2 in the SI), while silicified disks are partially exposed. After removal of organic substances by calcination at 500 °C in air, we found the silica skeleton of the epidermal layer (Fig. 2b, c, d). The skeleton is composed of silicified epidermal cell walls (Fig. 2e–h) and wedge-like structures ~8 μ m thick with a disk-shaped head ~10 μ m in diameter and a bottom ridge ~5 μ m in length (Fig. 2i–l). The silica wedges are located between the epidermal cells (Fig. S3 in the SI). We observed bottom ridges under the layer (Fig. 2k). The direction of the ridges on the reverse side of the epidermal layer is regularly arranged perpendicularly to the direction of elongation (Fig. S4 in the SI).

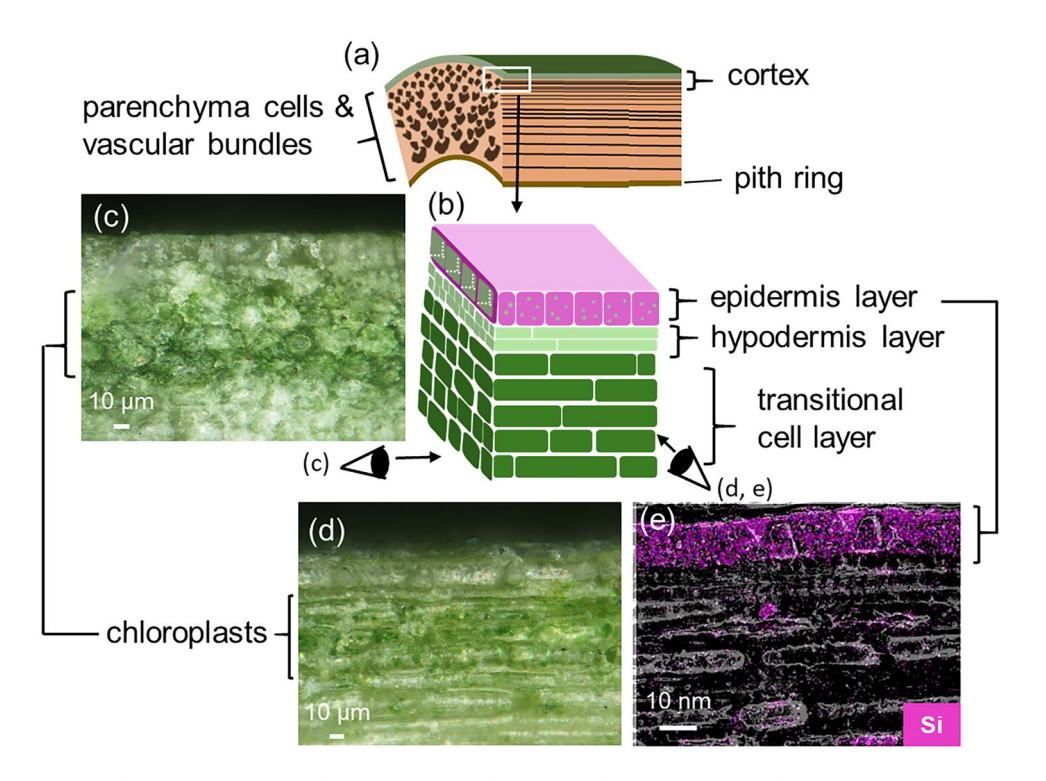


Fig. 1. Illustrations (\mathbf{a}, \mathbf{b}) and optical (\mathbf{c}, \mathbf{d}) and scanning electron micrograph (SEM) images with the elemental (Si) mapping (\mathbf{e}) of the cross sections of a culm wall of moso bamboo. The cross sections perpendicular (\mathbf{c}) and parallel (\mathbf{d}, \mathbf{e}) to the growth direction of the culm. Elliptical grains observed in the parenchyma are transitional layer cells (\mathbf{d}, \mathbf{e}) .

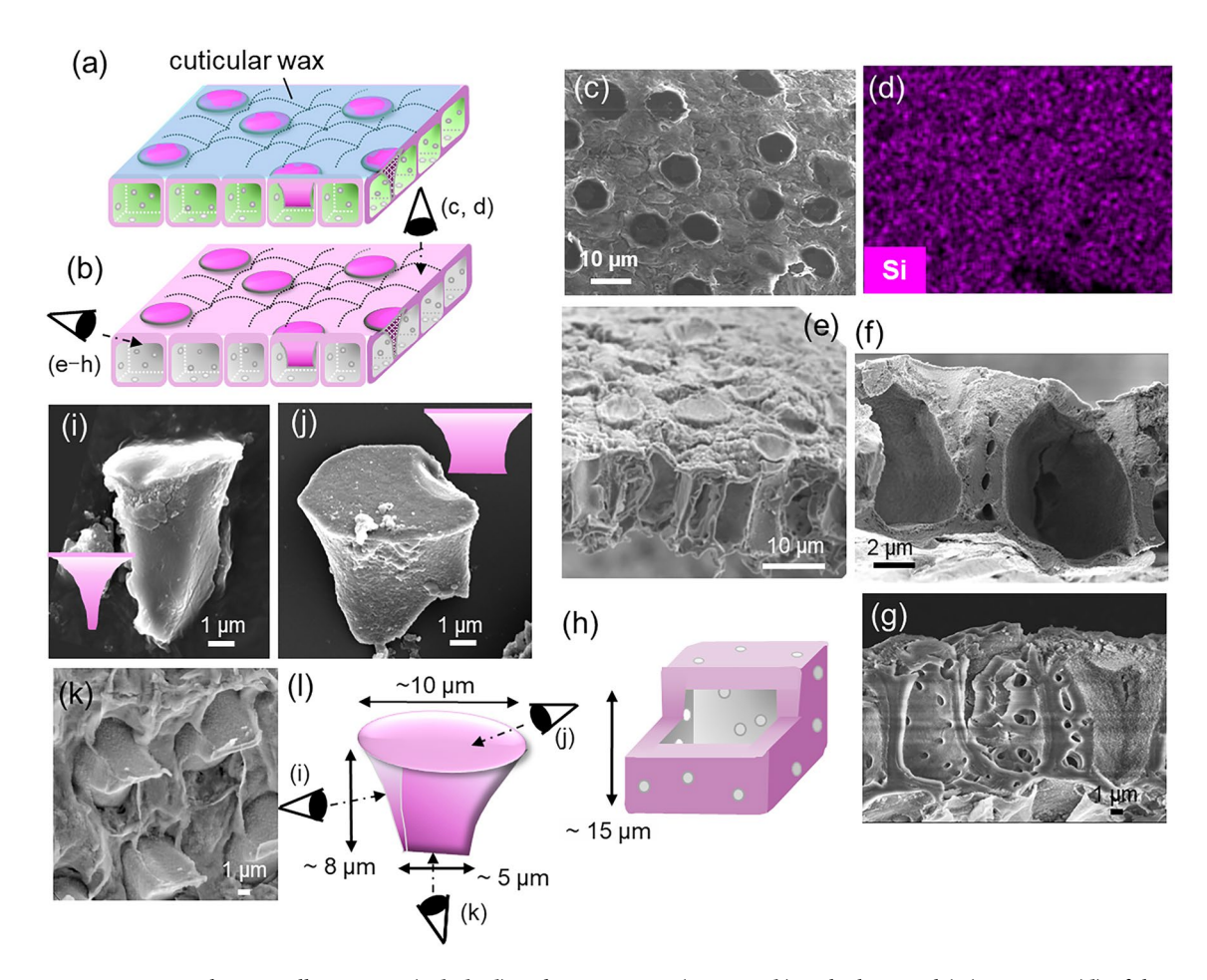


Fig. 2. Schematic illustrations (a, b, h, l) and SEM images (c, e-g, i-k) with elemental (Si) mapping (d) of the epidermal layers before (a) and after calcination (b-l). The surface (a-d), the epidermal cells (e-h), and the wedges (i-l). Pink areas indicate the presence of silica. Eye symbols indicate the direction of observation.

Nanometer-scale structures of two kinds of plant opals

Figure 3 shows schematic illustrations and SEM images of the silica wedges before and after partial removal of organic matter by chemical treatment with hypochlorite. As shown in Fig. 3a–c, we found small particles and fibrils on the crashed surfaces of untreated wedges. The fibrils were identified to as CNFs because they disappeared with treatment with cellulase, which is an enzyme that degrades cellulose (Fig. S5 in the SI). Thus, the silicas in the wedges are deduced to be a composite of silica nanoparticles and CNFs. The silica contents were roughly evaluated to be 80–90 wt% for the wedges by energy-dispersive X-ray spectroscopy (EDS) (Fig. S6 in the SI). After the removal of the organic matter, the wedges were found to be composed of particles 50–100 nm in diameter (Fig. 3d–f).

Figure 4 shows schematic illustrations and SEM images of the silica skeletons of the epidermal cells before and after partial removal of organic matter with chemical treatment. We observed large amounts of CNFs and small particles 30–50 nm in diameter before and after the treatment, respectively. Thus, the epidermal cell walls are also deduced to be a composite of silica nanoparticles and CNFs. The silica contents were roughly evaluated to be 40 wt% for silicified cells by energy-dispersive X-ray spectroscopy (EDS) (Fig. S6 in the SI).

Figure 5a shows FT-IR spectra of commercially available silica gel, cellulose, and plant opals of the epidermal layer after the removal of organic matter by a chemical treatment with hypochlorite. We found peaks of the C–O stretching (H), the C–OH stretching (I), the C–H bending (J), and the C–H bending (K) modes that are assigned to cellulose and absorption bands of the Si–O–Si stretching (A, B) and the Si–OH stretching (C) modes. Small signals of the N–H stretching (D), the C–H stretching (E), the N–H stretching (F), and the C–N stretching (G) modes were observed. Thus, the plant opals are deduced to contain CNFs and proteins or polyamines containing amine or amide.

The silica network was characterized by specific signals in the Raman spectra. Figure 5b shows the Raman spectra of commercially available silica gel, fused silica glass, and the plant opals of the epidermal layer after removal of organic matter by chemical treatment with a mixture of sulfuric and nitric acids. Since we found signals of the Si–O–Si stretching modes and the four-membered rings for all of the samples, the biological silicas have a fundamental Si–O–Si network similar to silica glass and silica gel. On the other hand, the absence of the three-membered rings and the presence of intense signals of the Si-OH stretching mode are recognized for the biosilicas and silica gel. Therefore, the plant opals were deduced to have a silica gel-like structure of

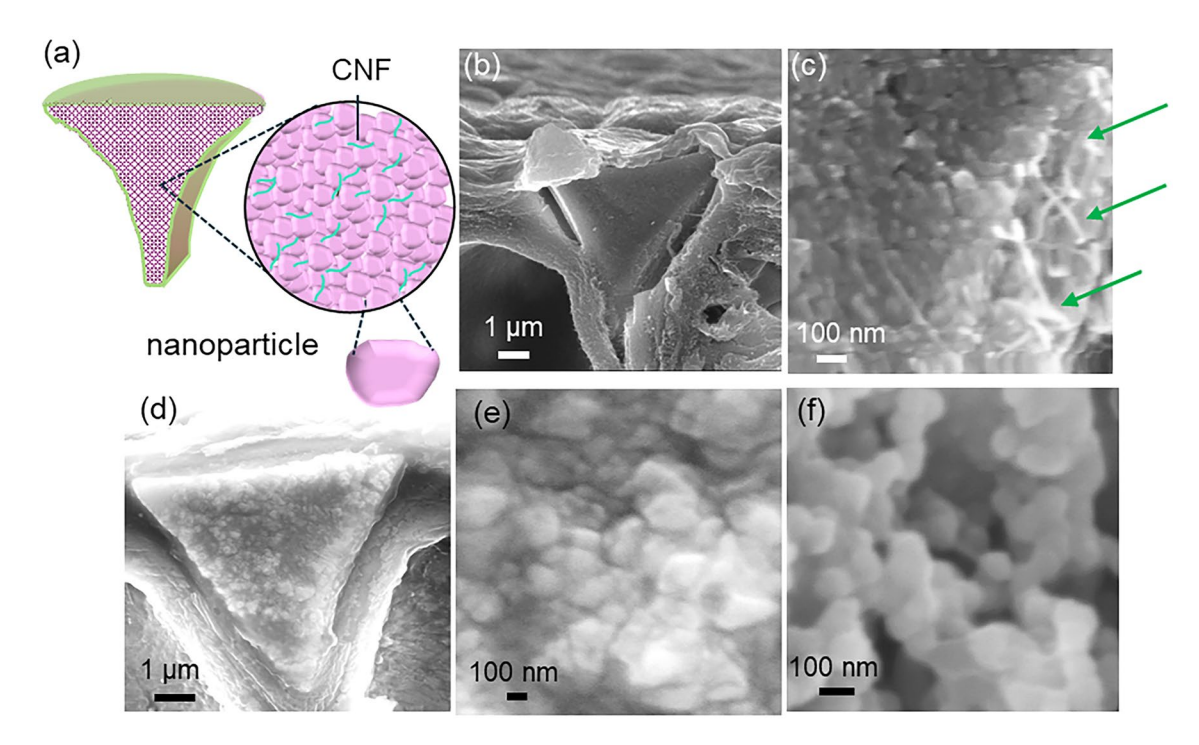


Fig. 3. Schematic illustration (a) and SEM images (b-f) of the silica skeletons for the wedge before (a-c) and after partial removal of organic matter with chemical treatments with hypochlorite (d-f). Green arrows indicate CNFs. The treatment periods were 1 (e) and 10 min (f).

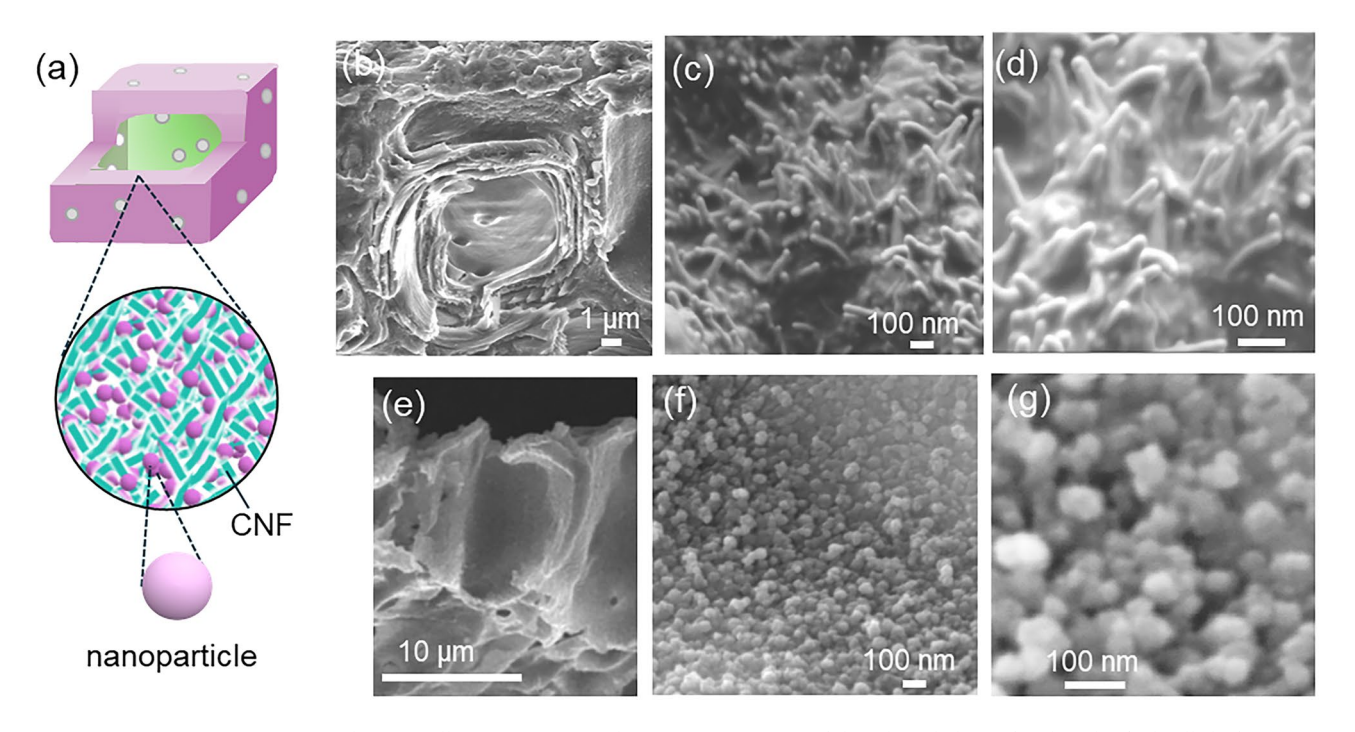


Fig. 4. Schematic illustrations (a) and SEM images (b-g) of the silica skeleton for the silicified cells before (a-d) and after (e-g) partial removal of organic matter with a chemical treatment with hypochlorite.

 $SiO_2 \cdot nH_2O$. As shown in Fig. S7 in the SI, the signal intensity of the Si–OH mode decreased and the signal of three-membered rings increased by heating of the plant opals to 800 °C in air. This supports the conclusion that the polycondensation of the Si–OH bonds in the biosilicas and silica gel resulted in the formation of the ring structure similar to that of silica glass.

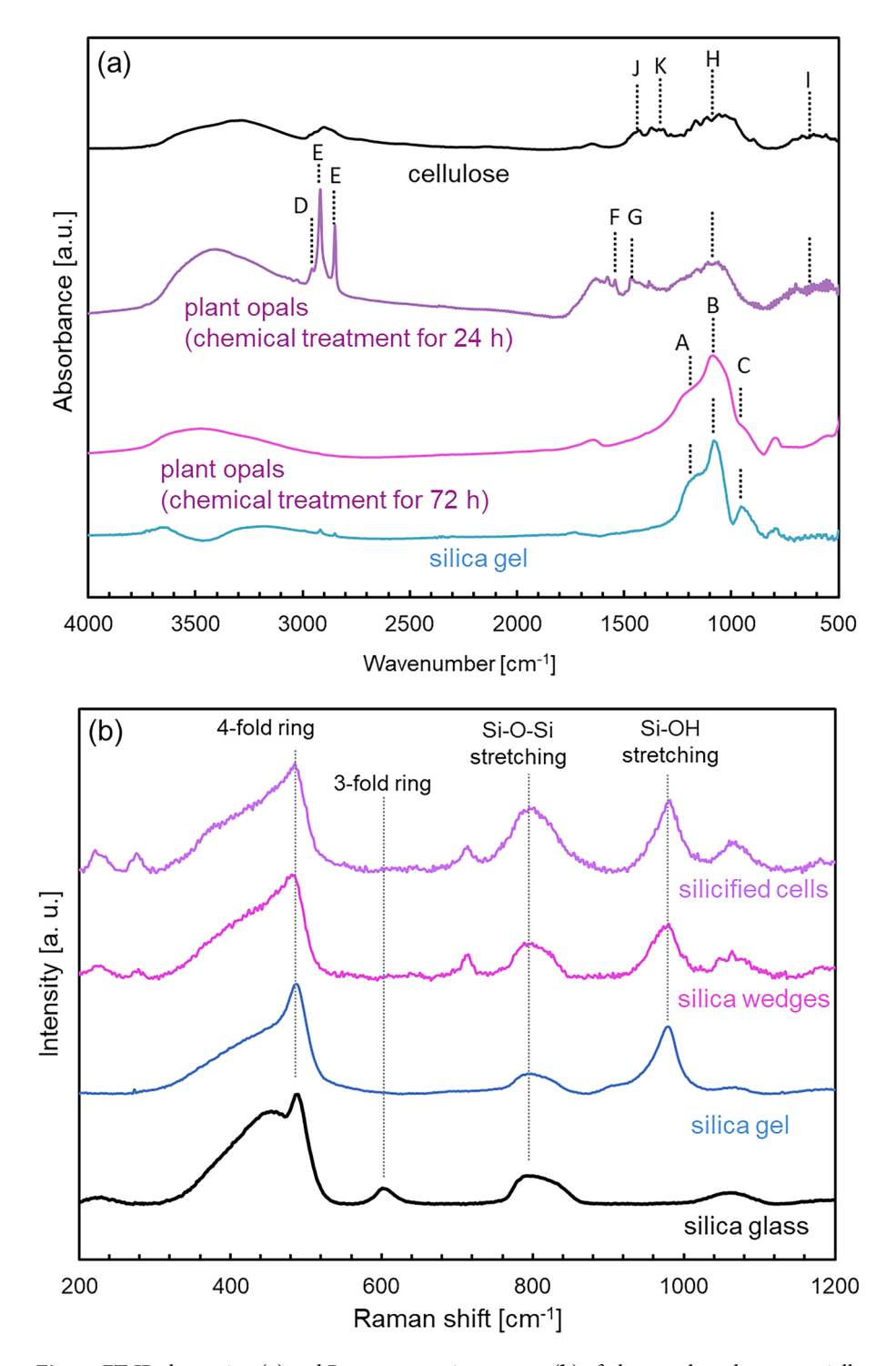


Fig. 5. FT-IR absorption (a) and Raman scattering spectra (b) of plant opals and commercially available silica gel (Kanto Chemical). A typical FT-IR spectrum of cellulose (Fujifilm Wako Pure Chemical) is shown in (a). We used plant opals of the epidermal layer after removal of organic matter by a chemical treatment with hypochlorite and a mixture of sulfuric and nitric acids for (a) and (b), respectively. A: the Si–O–Si stretching TO mode (1200 cm⁻¹), B: the Si–O–Si stretching LO mode (1060 cm⁻¹), C: the Si–OH stretching mode (950 cm⁻¹), D: the N–H stretching mode (2950 cm⁻¹), E: the C–H stretching mode (2848 and 2917 cm⁻¹), F: the N–H stretching mode (1540 cm⁻¹), G: the C–N stretching mode (1460 cm⁻¹), H: the C–O stretching mode (1030–1050 cm⁻¹), I: the C–OH stretching mode (660 cm⁻¹), J: the C–H bending mode (1430 cm⁻¹), K: the C–H bending mode (1315 cm⁻¹)^{28–32}. Broad absorption bands around 3200–3500 and 1600 cm⁻¹ are assigned to the H–O–H bending and the O–H stretching modes, respectively. A typical Raman spectrum of silica glass and assignments of the signals are shown in (b)^{32–34}.

We evaluated the mechanical properties of the biosilicas of the epidermal layer using the nanoindentation test. Figure S8 in the SI shows mapping images of the hardness and Young's modulus on the cross section parallel to the elongation direction of the epidermal layer. The hardness (H: ~2 GPa) and Young's modulus (E: ~20 GPa) of the silica wedges are higher than those (H: ~1 GPa, E: ~10 GPa) of the silicified cell walls. These results are consistent with a previous report³⁵. The mechanical properties of the silica wedge and the silicified cells are similar to those of the fan-shaped silicas and silica plates in rice leaves, respectively²¹. Basically, plant opals that are harder and tougher than organic frames protect the surface of the culms and leaves. However, the high-density parts having a specific morphology are assumed to have further specific functions. Since the fan-shaped silicas were reported to have an optical property for photosynthesis in rice plants²⁴, we focused the optical functions of the silica wedges in bamboo culms. Unfortunately, characterization of optical functions of small plant opals ~10 µm has been difficult by conventional techniques. Thus, we study the optical property of the silica wedges using numerical simulation in the later section.

Formation processes of two kinds of plant opals

We monitored the formation of plant opals of the epidermal layer of bamboo shoots and culm walls several weeks after emergence. At the initial stage in a week, the surface of a culm was not silicified (Fig. 6a–c). Silica wedges with a disk-shaped head were formed on the bamboo shoots two weeks after emergence (Fig. 6d–f). These bamboo shoots were not found to be covered with organic matter, such as cuticular wax. Silica accumulation was then observed on the epidermal cells for 16 weeks (Fig. 6g–i). Therefore, the wedges are rapidly formed within a few weeks and the epidermal cells are subsequently silicified within several months (Fig. S9 in the SI).

Figure 7 shows the silicification process of the wedges. We found the presence of a wedge-shaped organic frame before the formation of silica wedges on the culm of the 5th internode (Fig. 7a–e). Cotton-like CNFs were observed in the frame. Subsequently, silica nanoparticles were gradually accumulated from the wall of the frame on the culm of the 3rd internode (Fig. 7f–i). Finally, silica nanoparticles were filled with CNFs as a scaffold on the culm of the first internode (Fig. 7j–m). In rice leaf blades, silica nanoparticles 20–50 nm in diameter are deposited in the framework of the CNFs as a scaffold for mineral accumulation¹⁹. Specific morphologies, such as wedge-shaped silica in bamboo culms and fan-shaped silicas in rice leaves, are deduced to be controlled through the formation of silica nanoparticles on the CNF framework. Therefore, the intrafibrillar mineralization is regarded as a generalizable mechanism of biogenic silicification.

The epidermal layer cell walls were gradually silicified from the surface. Figure S9 in the SI shows the presence of epidermal cells in the middle of silicification. We observed the culm of the 20th and 30th internodes that

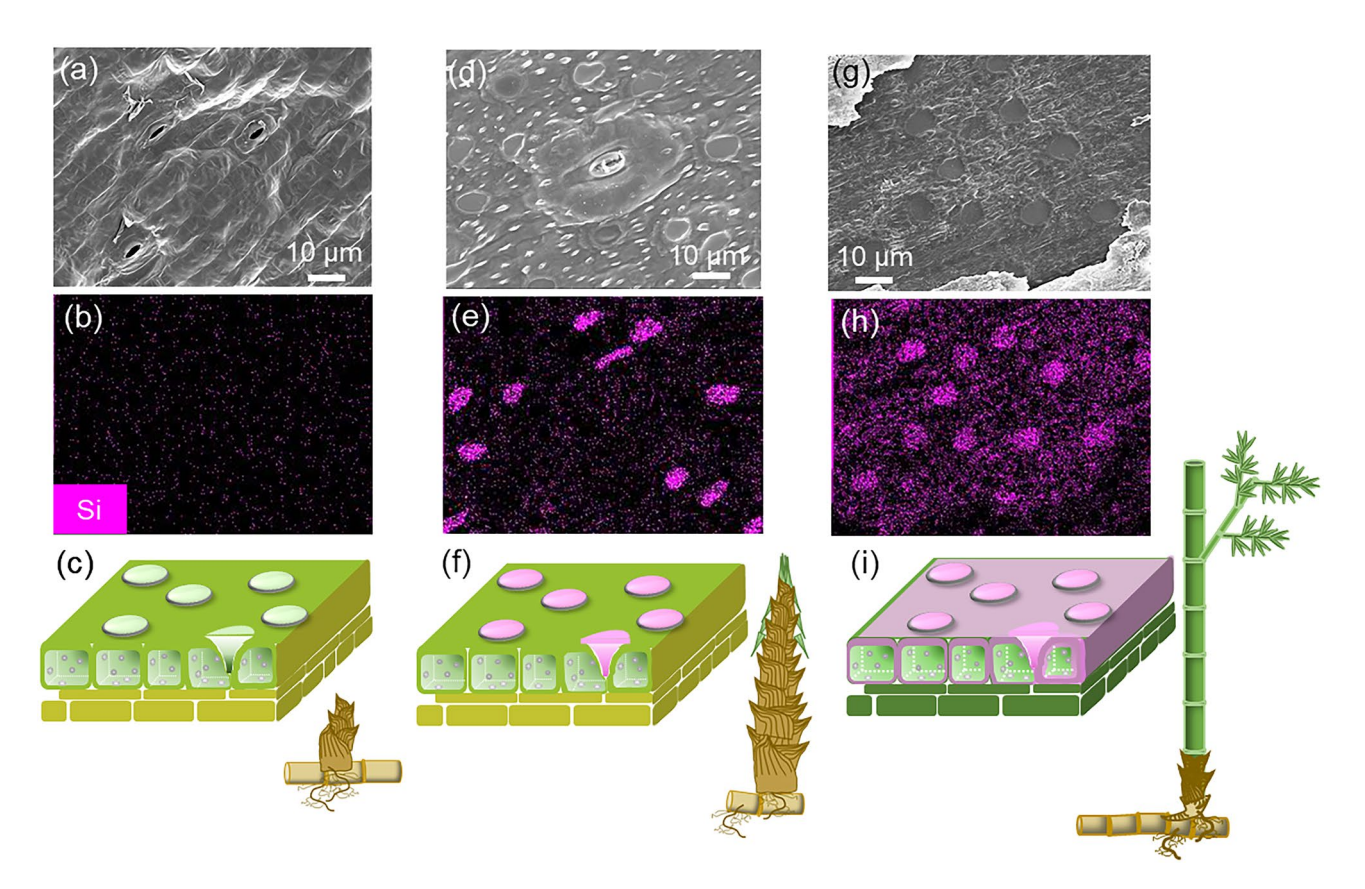


Fig. 6. SEM (a, d, g) and elemental (Si) mapping (b, e, h) images and schematic illustrations (c, f, i) of the surface of the epidermal layer of bamboo shoots and culm walls that grew for 1 (a-c), 2 (d-f), and 16 (g-i) weeks after emergence.

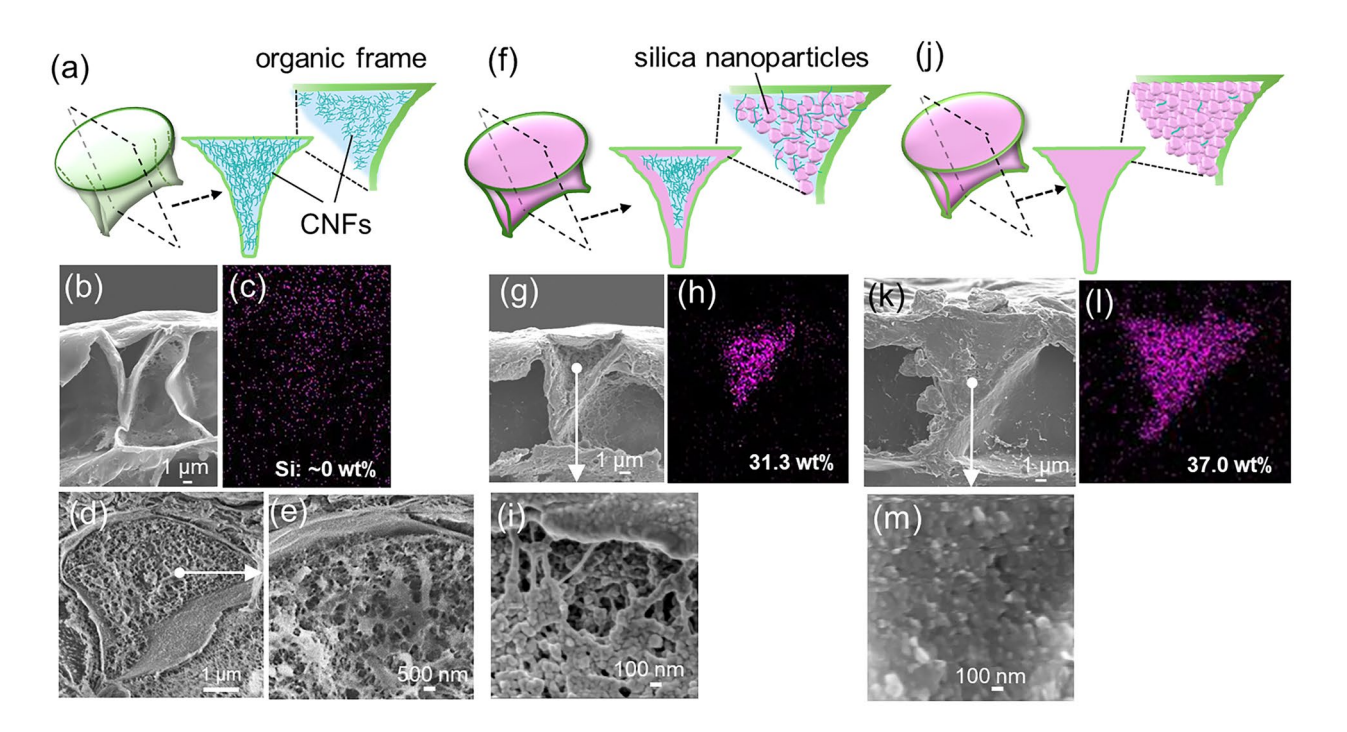


Fig. 7. Illustrations (a, f, j), SEM images (b, d, e, g, i, k, m), and elemental (Si) mapping (c, h, l) of the formation process of a wedge-shaped organic frame before (a-e) and after (f-m) the formation of the silica wedges. Internal structure observed from the cross section (b, g, i, k, m) of a wedge-shaped organic frame after critical drying. We observed the culm of the 1 st (j-m), 3rd (f-i), and 5th (a-e) internodes counting from the base of a bamboo shoot after two weeks from emergence on the ground.

grew for 4 months and 10th internodes that grew for 5 months after emergence. The epidermal cell walls were gradually silicified with nanoparticles and CNFs filling the voids in the cell walls.

Optical simulation of wedge-shaped Biosilicas

Numerical simulation was performed to evaluate the optical properties of silica wedge. Based on the actual geometry of biosilicas in the epidermal layer of a bamboo culm, a 3D model was created for a silica wedge 9 μm in height with a bottom ridge 5 μm in length with a round head 12 μm in diameter (Fig. S10 in the SI) to analyze the light path in the culm cortex near the silica wedge. As shown in Fig. 3(b, d), the wedge silica consists of densely packed nanoparticles. Since no significant submicron-scale heterogeneity was found in the particle assembly, we performed the optical simulation using a model having uniform silica composition and refractive index. Figure 8 shows the light intensity map through the wedge silica obtained by the beam propagation method (BPM). The incident beam focuses on the bottom ridge of the wedge, and then the light diffuses under the wedge regardless of the position of the light source and the incident angle. Although slight inhomogeneity of the refractive index and the wedge shape may broaden the beam, the diffusion of the light under the wedge is deduced to be basically achieved. Thus, natural sunlight is effectively introduced into the region under the epidermal layer without scattering by the surface structure. As shown in Fig. 1, chloroplasts are located in the region ~30 µm deep from the surface. These results suggest that the disk-like head, wedge body, and bottom ridge perform as a collector of sunlight, a waveguide located between the epidermal cells, and a diffuser, respectively, in promoting photosynthesis. As mentioned above, the fan-shaped silicas were also reported to have a role in guiding light to chloroplasts for enhancement of photosynthesis in rice plants²⁴. Thus, these high-density plant opals having a specific morphology in bamboo and rice plants are deduced to have specific optical functions.

The rapid formation of silica wedge within a few weeks after emergence is advantageous for enhancing growth of the young plant body. Optical simulation for the silicified epidermal cells was not performed because the difference in the refractive index is not sufficient for light control. In the near future, further experiments are needed to validate the proposed optical function although characterization of optical functions of small plant opals $\sim 10~\mu m$ has been difficult by conventional techniques.

Conclusion

The entire surface of moso bamboo culms was found to be covered with a microscopic structure of two types of silica: silicified epidermal cell walls and silica wedge with a discoid head. Detailed analysis revealed that they were composed of silica nanoparticles and cellulose nanofibrils. Numerical simulations revealed that the silica wedge has an optical function that redistributes the light intensity internally through the culm.

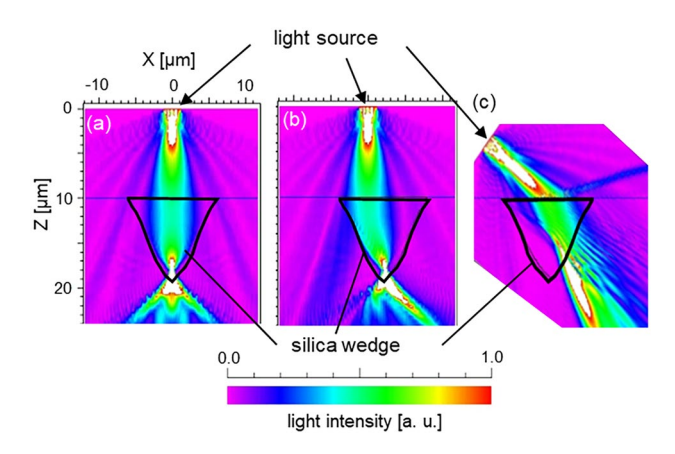


Fig. 8. Light intensity maps through silica wedges obtained by the BPM. The beams are emitted from the light source located at the central axis of the wedge for the vertical direction (**a**) and off-axis for the vertical direction (**b**) and the oblique direction (**c**). The conditions for the numerical simulation are shown in Fig. S10 in the SI. The light wavelength was set at 660 nm¹, which is the maximum absorption wavelength for chloroplast. The refractive indices (n) of biosilicas and the matrix of a culm cortex were approximated by the value of amorphous silicas (n = 1.46) and by the average value of water and plant cells (n = 1.425), respectively. The incident beam diameter at the top surface of the wedge (at Z = 10 μm) was ~6 μm. The input light was assumed to be a circular beam with uniform intensity within the beam cross section. The vertical beam focuses on the bottom ridge of the wedge, and then the light diffuses under the wedge (a, b). The oblique beam is also introduced into the region under the wedge (**c**).

Methods

Culms and shoots of moso bamboo (*P. edulis*) that grew in the current year were sampled in Yokohama, Japan. The collection was permitted by Keio University, the land owner and the authors' affiliation. These samples, which were identified by Chikako Hasekura, one of the co-authors, are deposited as scientific voucher specimens (catalog number: KPM-NA0222430, KPM-NA0222431) at the Kanagawa Prefectural Museum of Natural History.

The culm walls near the cortex were sectioned using a saw and further trimmed into pieces (~ 20 mm x ~ 20 mm) with a scalpel. The radial and cross-sections near the cortex were observed using an optical microscope (Keyence VH-Z500R). Cuticular wax was removed using a sodium hypochlorite solution at pH 5. Small blocks of culm walls near the cortex were embedded in epoxy resin (Nihon-Resin) and polished with waterproof abrasive papers to expose radial surfaces.

A tissue sample ($\sim 100~\mu m$ thick) from the cortex region of culm walls was carefully peeled and trimmed into thin sections ($\sim 5~mm \times \sim 20~mm$, 1–2 mm thick). These sections were immersed in a 0.1 M phosphate buffer solution at pH 6.8 containing cellulase (Onozuka RS from *Trichoderma viride*, $\sim 2~U/mg$). The mixture was incubated at 60 °C for 48 h. After enzymatic treatment, the samples were washed with purified water and freeze-dried.

A \sim 100 μ m-thick tissue sample from the cortex region was ground into small fragments using a grinder. These fragments were subjected to thermal treatment at 350 °C for 3 h in air to carbonize organic components. The carbonized parts were washed to eliminate alkaline metals and residual organics. Subsequent heat treatment at 500 °C for 5 h was performed to completely remove organic matter.

Bamboo shoots were fixed immediately after collection in 2.5% glutaraldehyde (Fuji Film Wako) solution prepared with 0.1 M phosphate buffer. The fixed samples were washed with the phosphate buffer. Ethanol dehydration was conducted using a graded ethanol series (30%, 50%, 70%, 80%, 90%, 95%, and 100%). The samples were then subjected to supercritical drying using a CO₂ supercritical dryer (Leica EM CPD300).

The prepared samples were coated with osmium for detailed surface and cross-sectional observations using a scanning electron microscope (SEM; JEOL JSM-7600 F, Merlin compact, JSM-IT700HR/LA) operated at an acceleration voltage of 5–10 kV. For bamboo shoots in the pre-formation stage of silica wedges, cryogenic fracturing with solid nitrogen was performed, followed by observation using cryo SEM (Hitachi S-3400 N).

For isolation of biosilicas, cortex tissues were ground using a blender and were filtered through a nylon mesh (Bolting Cloth Mesh 60). The filtrate was transferred to a watch glass and subjected to centrifugation. The residue was collected and purified by further centrifugation in a saturated CsCl and CaCl₂ solution (ρ = 1.75). Additional treatment with sodium hypochlorite at pH 5 was performed for further purification of biosilicas. The isolated biosilicas were analyzed using FT–IR (Jasco, FT/IR-4200).

Nanoindentation was performed using a KLA iMicro Nanoindenter with a Berkovich indenter tip. The mapping images were obtained from polished radial surfaces of bamboo culm walls that were embedded in epoxy resin. Hardness and Young's modulus were calculated using the Oliver and Pherr method³⁶.

In a separate protocol, cortex tissues were treated with a mixed acid solution (96% sulfuric acid: 60% nitric acid = 3:1, Kanto Chemical) for 48 h to eliminate organic matter. Resultant biosilicas were washed with purified water, recovered, and dried. Gold nanoparticles (20 nm in diameter; Merck, OD 1, citrate buffer-stabilized suspension)

were applied to enhance surface plasmon effects for Raman analysis. The purified biosilicas were analyzed using micro-Raman spectroscopy with a laser confocal microscope (InVia Raman Microscope, Renishaw). A 532 nm excitation laser was focused on the sample surface using a $\times 100$ objective lens.

Data availability

The authors declare that the data supporting the findings of this study are available within the paper and its Supplementary Information file. Raw data files are available from the corresponding author upon reasonable request.

Received: 10 March 2025; Accepted: 11 June 2025

Published online: 01 July 2025

References

- 1. Wang, T., Antonietti, M. & Cölfen, H. Calcite mesocrystals: 'morphing' crystals by a polyelectrolyte. *Chem. Eur. J.* 12, 5722–5730 (2006).
- 2. Miyajima, R., Oaki, Y., Kogure, T. & Imai, H. Variation in mesoscopic textures of biogenic and biomimetic calcite crystals. *Cryst. Growth Des.* 15, 3755–3761 (2015).
- 3. Owari, Y. et al. Ultrastructure of setae of a planktonic diatom, Chaetoceros coarctatus. Sci. Rep. 12, 7568 (2022).
- 4. Seto, J., Ma, Y., Davis, S. & Cölfen, H. Structure-property relationships of a biological mesocrystal in the adult sea urchin spine. *Proc. Natl. Acad. Sci. USA.* **109**, 3699–3704 (2012).
- 5. Ehrlich, H. Chitin and collagen as universal and alternative templates in biomineralization. Int. Geol. Rev. 52, 661-699 (2010).
- Gordon, R., Losic, D., Tiffany, M. A., Nagy, S. S. & Sterrenburg, F. A. The glass menagerie: diatoms for novel applications in nanotechnology. *Trends Biotechnol.* 27, 116–127 (2009).
- 7. Hildebrand, M. Diatoms, biomineralization processes, and genomics. Chem. Rev. 108, 4855-4874 (2008).
- 8. Kröger, N. & Poulsen, N. Diatoms From cell wall biogenesis to nanotechnology. Annu. Rev. Genet. 42, 83–107 (2008).
- 9. Kröger, N., Deutzmann, R. & Sumper, M. Polycationic peptides from diatom Biosilica that direct silica nanosphere formation. *Science* **286**, 1129–1132 (1999).
- 10. Coradin, T. & Lopez, P. J. Biogenic silica patterning: Simple chemistry or subtle biology? ChemBioChem 4, 251-259 (2003).
- 11. Foo, C. W. P., Huang, J. & Kaplan, D. L. Lessons from seashells: silica mineralization via protein templating. *Trends Biotechnol.* 22, 577–585 (2004).
- 12. Pisera, A. et al. Insights into the structure and morphogenesis of the giant basal spicule of the glass sponge Monorhaphis chuni. *Front. Zool.* 18, 58 (2021).
- 13. Müller, W. E. G. et al. Bioorganic/inorganic hybrid composition of sponge spicules: matrix of the giant spicules and of the comitalia of the deep sea hexactinellid Monorhaphis. *J. Struct. Biol.* **161**, 188–203 (2008).
- Weaver, J. C. et al. Hierarchical assembly of the siliceous skeletal lattice of the hexactinellid sponge Euplectella aspergillum. J. Struct. Biol. 158, 93-106 (2007).
- 15. Sandford, F. Physical and chemical analysis of the siliceous skeletons in six sponges of two groups (demospongiae and hexactinellida). *Microsc Res. Tech.* **62**, 336–355 (2003).
- 16. Nakamura, Y., Suzuki, N. & Phaeodaria Diverse marine cercozoans of World-Wide distribution. in *Marine Protists: Diversity and Dynamics* (ed. Ohtsuka, S., Suzaki, S., Horiguchi, T., Suzuki, N., Not, F.) 223–249 (*Springer Tokyo*, (2015).
- 17. Nakamura, Y. et al. Elemental composition and ultrafine structure of the skeleton in shell-bearing protists—A case study of phaeodarians and radiolarians. *J. Struct. Biol.* **204**, 45–51 (2018).
- 18. Perry, C. C. & Fraser, M. A. Silica deposition and ultrastructure in the cell wall of Equisetum arvense: the importance of cell wall structures and flow control in biosilicification? *Philos. Trans. R Soc. Lond. B Biol. Sci.* **334**, 149–157 (1991).
- 19. Nakamura, E., Ozaki, N., Oaki, Y. & Imai, H. Cellulose intrafibrillar mineralization of biological silica in a rice plant. *Sci. Rep.* 11, 7886 (2021)
- 20. Ma, J. F. Role of silicon in enhancing the resistance of plants to biotic and abiotic stresses. Soil. Sci. Plant. Nutr. 50, 11-18 (2004).
- 21. Sato, K. et al. Effects of nanostructured Biosilica on rice plant mechanics. RSC Adv. 7, 13065–13071 (2017).
- Cvjetinovic, J. et al. Revealing the static and dynamic Nanomechanical properties of diatom frustules—Nature's glass lace. Sci. Rep. 13, 5518 (2023).
- 23. Monn, M. A., Vijaykumar, K., Kochiyama, S. & Kesari, H. Lamellar architectures in stiff biomaterials May not always be templates for enhancing toughness in composites. *Nat. Commun.* 11, 373 (2020).
- 24. Sato, K. et al. Optical properties of Biosilicas in rice plants. RSC Adv. 6, 109168–109173 (2016).
- Lux, A., Luxová, M., Abe, J., Morita, S. & Inanaga, S. Silicification of bamboo (Phyllostachys heterocycla Mitf.) root and leaf. Plant. Soil. 255, 85-91 (2003).
- 26. Li, S. H., Liu, Q., De Wijn, J. & Zhou, B. L. Calcium phosphate formation induced on silica in bamboo. *J. Mater. Sci. Mater. Med.* **8**, 427–433 (1997).
- 27. Cui, J., Jiang, M., Nicola, M., Masic, A. & Qin, Z. Multiscale Understanding in fracture resistance of bamboo skin. *Extreme Mech. Lett.* 49, 101480 (2021).
- 28. Su, J. F., Huang, Z., Yuan, X. Y., Wang, X. Y. & Li, M. Structure and properties of carboxymethyl cellulose/soy protein isolate blend edible films crosslinked by Maillard reactions. *Carbohydr. Polym.* **79**, 145–153 (2010).
- 29. Shabanpour, B., Kazemi, M., Ojagh, S. M. & Pourashouri, P. Bacterial cellulose nanofibers as reinforce in edible fish myofibrillar protein nanocomposite films. *Int. J. Biol. Macromol.* 117, 742–751 (2018).
- 30. Rubio, F., Rubio, J. & Oteo, J. L. A FT-IR study of the hydrolysis of tetraethylorthosilicate (TEOS). Spectrosc. Lett. 31, 199-219 (1998).
- 31. Kamitsos, E. I., Patsis, A. P. & Kordas, G. Infrared-Reflectance spectra of Heat-Treated, Sol-Gel-Derived silica. *Phys. Rev. B.* 48, 12499–12505 (1993).
- 32. Sato, Y., Hayami, R. & Gunji, T. Characterization of NMR, IR, and Raman spectra for siloxanes and silsesquioxanes: A Mini review. *J. Sol-Gel Sci. Technol.* **104**, 36–52 (2022).
- 33. Stolen, R. H. & Walrafen, G. E. Water and its relation to broken bond defects in fused silica. J. Chem. Phys. 64, 2623-2631 (1976).
- 34. Barrio, R. A., Galeener, F. I., Martinez, E. & Elliott, R. J. Regular ring dynamics in AX₂ tetrahedral glasses. *Phys. Rev. B.* 48, 15672–15689 (1993).
- 35. Yu, Z., Jiang, Z., Zhang, X. & Yu, Y. Mechanical properties of silica cells in bamboo measured using in nanoindentation. *Wood Fiber Sci.* 48, 228–233 (2016).
- 36. Oliver, W. & Pharr, G. Measurement of hardness and elastic modulus by instrumented indentation: advances in Understanding and refinements to methodology. *J. Mater. Res.* 19, 3–20 (2004).

Acknowledgements

This work was financially supported by JSPS KAKENHI grant number 21H01627 (23K21040).

Author contributions

H. I. supervised the project. M. K., H. W., Y. O., and H. I. designed the experimental procedure of microstructure analysis. C. H. identified moso bamboo and provided biological knowledge of bamboo. M. K., T. W. and T. I. constructed models of plant opal and numerical simulations. All authors reviewed the manuscript.

Competing interests

The authors declare no competing interests.

Additional information

Supplementary Information The online version contains supplementary material available at https://doi.org/1 0.1038/s41598-025-06906-w.

Correspondence and requests for materials should be addressed to H.I.

Reprints and permissions information is available at www.nature.com/reprints.

Publisher's note Springer Nature remains neutral with regard to jurisdictional claims in published maps and institutional affiliations.

Open Access This article is licensed under a Creative Commons Attribution-NonCommercial-NoDerivatives 4.0 International License, which permits any non-commercial use, sharing, distribution and reproduction in any medium or format, as long as you give appropriate credit to the original author(s) and the source, provide a link to the Creative Commons licence, and indicate if you modified the licensed material. You do not have permission under this licence to share adapted material derived from this article or parts of it. The images or other third party material in this article are included in the article's Creative Commons licence, unless indicated otherwise in a credit line to the material. If material is not included in the article's Creative Commons licence and your intended use is not permitted by statutory regulation or exceeds the permitted use, you will need to obtain permission directly from the copyright holder. To view a copy of this licence, visit http://creativecommons.org/licenses/by-nc-nd/4.0/.

© The Author(s) 2025